# Elucidation of Li$^+$ Conduction Behavior in MOF Glass Electrolyte Toward Long-Cycling and High C-Rate Lithium Metal Batteries

*Ourui Kong, Guangshen Jiang,* Kun Wang, Anping Yang, Jingang Zheng, Shuai Wu, Weichen Han, Jijia Li, Lichao Li, Xilong An, Jin Wang, Chengguo Sun, Lixiang Li, Fei Xu,* and Baigang An**

**Vitrified metal–organic frameworks (MOFs) are promising solid-state electrolytes for lithium metal batteries due to their unique structures. Nevertheless, the effect of distorted molecular structures in glassy MOFs on Li$^+$ migration behavior at the molecular level remains largely unexplored, posing a huge obstacle to further boosting their electrochemical performances. Herein, Li$^+$ conduction behavior in glassy ZIF-62 quasi-solid-state electrolyte (GZ-62-QSSE) is molecularly elucidated, in which Li$^+$ migration is accomplished by the continuous delivery of N sites in imidazole and benzimidazole ligands like the process of relay race. Such fast Li$^+$ migration in GZ-62-QSSE demonstrates more than 1.5-time increase in transference number and helps to generate inorganic-dominated cathode/anode interphases for unblocked ion transport compared with crystalline ZIF-62 electrolyte. Consequently, the long-term stability with remarkable high-rate capability is realized in the proof-of-the-concept full cells, which represents one of best values among all reported MOF-based solid-state batteries. For example, LiFePO$_4$ ||Li full cells employing GZ-62-QSSE brilliantly undergo 3000 cycles with high initial capacity of 132.1 mAh g$^{-1}$ and ultralow decay rate of 0.009% at 1 C. Full cells still display high discharge capacity of 83.6 mAh g$^{-1}$ at 5 C. The elaborated high-performance glassy ZIF-62 electrolyte offers new insights for exploiting advanced solid-state electrolytes and propels the development of solid-state lithium metal batteries.**

## 1. Introduction

The pressing demands for high-energy-density and high-safety lithium metal batteries (LMBs) stimulate tremendous attempts in exploring the state-of-art solid-state electrolytes (SSEs).[1] Among the exploited SSEs, glassy materials have been substantiated as very prospective candidates.[2] As a brand-new member of the glass family, vitrified metal-organic frameworks (MOFs) are amorphous coordination polymers, which are located in the metastable state in the energy aspect and long-range disorder at the microstructure level.[3] As SSEs, they indeed delivered fast transport kinetics, excellent ionic conductivity, and good dendrite suppression in solid-state LMBs, which were simply ascribed to the isotropy,[4] boundary-free attributes[5] and disordered network structure[6] of MOF glass. The ionic migration ability was merely quantitatively evaluated by the ionic diffusion coefficients of MOF glass.[5] Obviously, these understandings still stay at structural traits of MOF glass on the macro level and do not provide insightful molecular information over how Li$^+$ migrates. Accordingly, deeper insight into Li$^+$ migration at the molecular level in MOF glass remains elusive, which cannot effectively guide the design of high-performance vitrified MOF-based SSEs. Therefore, it is of paramount significance and urgence to probe cationic conduction behavior in glassy MOFs.

Apart from the undiscovered mechanism over ionic conduction behavior, the electrochemical performance of full cells

---

O. Kong, G. Jiang, K. Wang, J. Zheng, S. Wu, W. Han, J. Li, L. Li, X. An, C. Sun, L. Li, B. An
School of Chemical Engineering
University of Science and Technology Liaoning
Anshan, Liaoning 114051, P. R. China
E-mail: jianggsh@ustl.edu.cn; bgan@ustl.edu.cn

A. Yang, F. Xu
State Key Laboratory of Solidification Processing
School of Materials Science and Engineering Shaanxi Joint Laboratory of Graphene (NPU)
Northwestern Polytechnical University
710072
Xi'an, P. R. China
E-mail: feixu@nwpu.edu.cn

J. Wang
Wanhua Chemical Group Co. Ltd
Yantai, Shandong 264002, P. R. China

The ORCID identification number(s) for the author(s) of this article can be found under https://doi.org/10.1002/aenm.202405593

**DOI: 10.1002/aenm.202405593**

equipped with MOF glass SSE also needs to be further boosted. Although recent attempts over the vitrified ZIF-4 and ZIF-62-based SSEs validated their effectiveness, the cycling lifespans of full cells paired with $LiFePO_4$ (LFP) were no more than 1500 cycles.[6a,7] Meanwhile, the rate performanceswere quite low, showing a capacity of less than 65 mAh $g^{-1}$ at 5 C-rate.[8] Hence, there is plenty of room to enhance the electrochemical performance of batteries. As is well known, the performances not only rely on SSE but also depend on electrode/electrolyte interphases, such as solid electrolyte interphase (SEI) and cathodic electrolyte interphase (CEI). It is widely accepted that rich inorganics like LiF can intensify ionic transport and rigidity, and a small quantity of organic components enhance the resilience of SEI and CEI layers.[9] We envision that the elaborate construction of MOF glass electrolyte with rational composition-distribution SEI and CEI permits further huge advance of cell performance. In this case, the current performance toward long-term lifespan over 3000 cycles and high C-rate capacity over 80 mAh $g^{-1}$ (at 5 C) has been scarcely explored.

Herein, we initially investigate the $Li^+$ conduction behavior at a molecular level in vitrified ZIF-62 as a typical example of MOFs glass and discover the "relay race"-style migration behavior for the first time. Admirable ZIF-62 glass quasi-solid-state electrolyte (GZ-62-QSSE), generating a cascade structure consisting of inorganic-dominated SEI and CEI with Li anode and cathode, is fabricated for high-performance and long-lifespan LMBs. Relying on N species in the deformed coordination environment from ZIF-62 glass, GZ-62-QSSE demonstrates a high conductivity of $3.32 \times 10^{-4}$ S $cm^{-1}$ at 20 °C with $Li^+$ transference number ($t^+$) of 0.74 and the remarkable compatibility with Li anode. Bearing a wide electrochemical stable window up to 4.8 V, GZ-62-QSSE can match with LFP and $LiNi_{0.8}Co_{0.1}Mn_{0.1}O_2$ (NCM811) cathodes. Especially, high initial capacities of 132.1 and 154.5 mAh $g^{-1}$ are achieved in the full cells employing GZ-62-QSSE with cycling lifespans of 3000 and 700 times at 1 C for LFP and NCM811, respectively. Impressively, full cells still display high discharge capacities of 83.6 and 105.1 mAh $g^{-1}$ at 5 C. Our study over the vitrified ZIF-62 electrolyte provides a new understanding of ion conduction in MOF glass and an avenue to exploiting advanced solid-state LMBs.

## 2. Results and Discussion

In-depth insights into ion transport mechanism in MOF glass are of vital importance for instructing the design and exploration of SSEs. Taking ZIF-62 glass and ZIF-62 crystal for instance, the simulated probability distributions of Li position according to ab initial molecular dynamics (AIMD) are revealed in **Figure 1**a,b. In the ZIF-62 crystal unit cell, $Li^+$ motion space is severely restricted in local domains, while the migration space expands to a larger one in ZIF-62 glass due to the homogeneity, intrinsic defects, and free volume of glass.[2b] The mean square displacements (MSD) of $Li^+$ in these two materials are recorded in Figure 1c. The calculated ionic diffusivity according to the overall slope of ZIF-62 glass is $3.97 \times 10^{-9}$ $m^2$ $s^{-1}$, evidently greater than that of the crystalline counterpart ($1.43 \times 10^{-9}$ $m^2$ $s^{-1}$). These apparently verify that the glass phase promotes ion diffusion along continuous and homogeneous transport channels compared with crystalline polymorphs. As shown in Videos S1 and S2 (Supporting information) for ZIF-62 glass and ZIF-62 crystal, $Li^+$ possibly acts as a relay baton and N sites from imidazole and benzimidazole ligands as athletes like relay race. Therefore, $Li^+$ conduction is accomplished through the dynamic delivery of N sites in ZIF-62. The snapshots from the AIMD simulation vividly depict $Li^+$ migration behavior in the imidazolate frameworks. The $Li^+$ migration distance is estimated to be 3.92 Å (starting from 2.21 to 6.13 Å) for ZIF-62 glass, whereas the distance in ZIF-62 crystal is 1.49 Å (from 4.23 to 5.72 Å) (Figure 1d,e). They demonstrate $Li^+$ in ZIF-62 glass transfer faster than in ZIF-62 crystal within the same simulation time frame. To further unravel the reason for the above phenomenon, $Li^+$ movement trajectories in ZIF-62 crystal and ZIF-62 glass segments are shown in Figure 1f,g. In ZIF-62 crystal, $Li^+$ motion densely surrounds N species and is relatively isolated, whereas the continuous $Li^+$ migration along N atoms is observed in ZIF-62 glass, indicative of high ionic conductivity within MOF glass. The corresponding radial distribution functions (RDF) of Li—N bond lengths are counted and portrayed in Figure 1h. For the ZIF-62 crystal, the Li—N bond length is concentrated at 2.14 Å, which represents that $Li^+$ are constrained by N species from imidazole and benzimidazole linkers with intensive interaction. Similarly, a Li—N bond length of 2.22 Å is also observed in ZIF-62 glass (Figure 1g). The shorter Li—N bond in the ZIF-62 crystal implies that $Li^+$ is bound more tightly by N species and $Li^+$ migration becomes more difficult. In comparison, a long Li—N bond means that $Li^+$ is facile to be detached from N species with weak interaction in ZIF-62 glass, embodying the low activation energy ($E_a$) as mentioned below. The discrepancy among N species in ZIF-62 crystal and ZIF-62 glass originates from the disparity in the chemical coordination environment because of the structural deformation of ZIF-62 glass,[10] as further discussed below. These above-mentioned results illustrate that $Li^+$ transport is accelerated by N species in distorted structure from ZIF-62 glass like relay race. The previous reports are simply attributed to the unique attributes and the disordered network structure of ZIF glass or the structural design of composite SSE on the macro level for enhancing ionic conductivity.[6a,7] In term of study scales, the above-mentioned $Li^+$ conduction behavior vastly differentiates from the other ZIF-62 glassy-based SSEs.

ZIF-62 glass is derived from the crystalline counterpart through a typical melt-quenching approach. The molecular structure models of the crystalline and glassy ZIF-62 are separately present in **Figure 2**a,b. The synthesized crystalline ZIF-62 via the solvothermal method has an identical X-ray diffraction (XRD) pattern with the simulated ZIF-62, as revealed in Figure 2c, demonstrating the pure phase of the as-obtained sample. After heat treatment, the vitrified ZIF-62 shows the amorphous trait verified by two broad peaks in the XRD pattern.[11] To corroborate the vitrification occurrence of crystalline ZIF-62 during heat treatment, differential scanning calorimetry (DSC) was carried out. During upscan 1, the peaks at 327 and 465 °C are seperately attributed to the desolvation and

---

C. Sun
School of Chemical Engineering
Nanjing University of Science and Technology
Nanjing, Jiangsu 210094, P. R. China

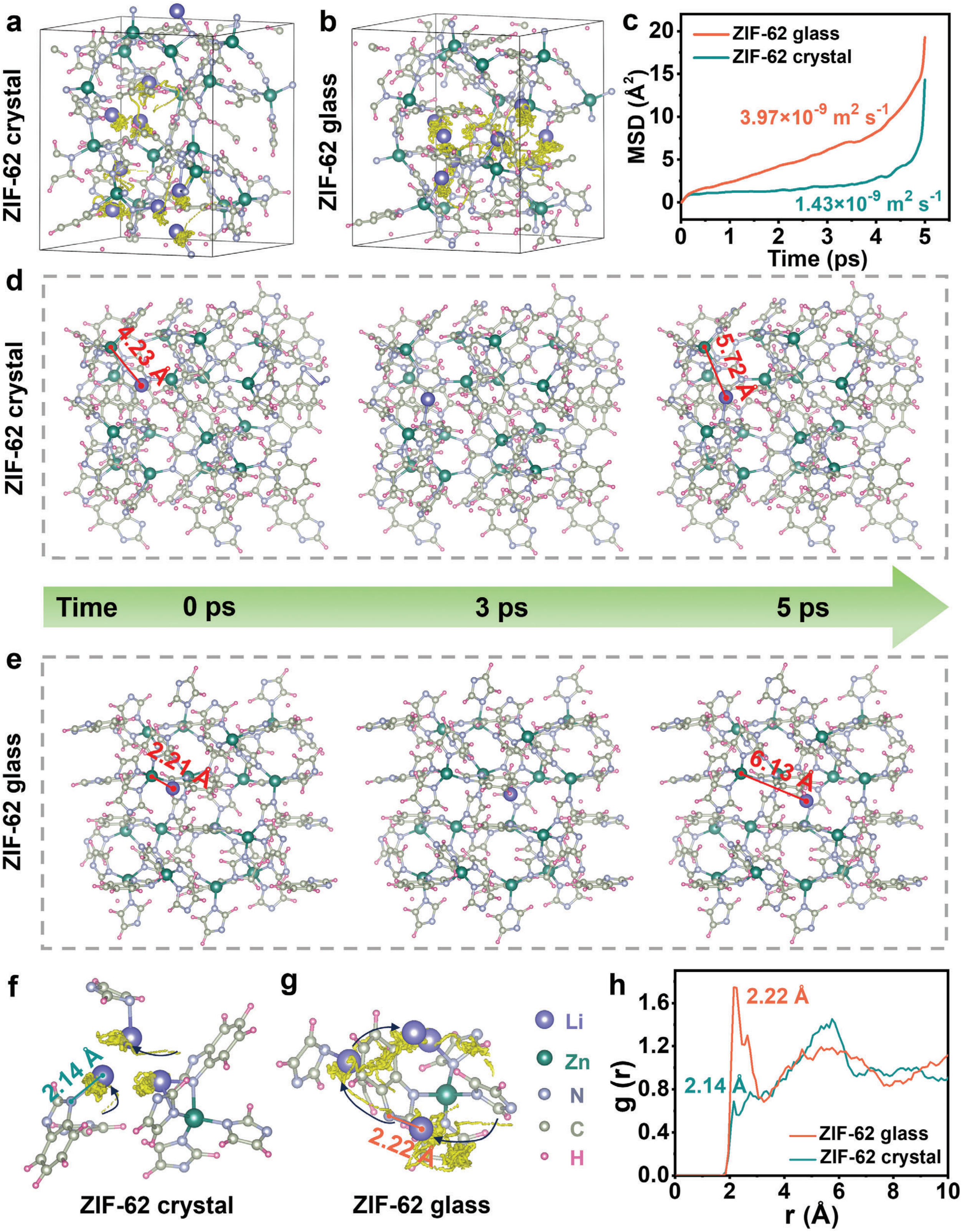

**Figure 1.** Atom position distribution of Li in a) ZIF-62 crystal and b) ZIF-62 glass; c) Li MSD in crystalline and glassy ZIF-62 during 5 ps; d,e) Structural snapshots of $Li^+$ migration in ZIF-62 crystal and ZIF-62 glass from AIMD simulations; Movement trajectories of Li element in f) ZIF-62 crystal and g) ZIF-62 glass; h) RDF of Li-N in ZIF-62 crystal and ZIF-62 glass. The yellow curves in a, b, f and g represent the movement trajectories of Li ions.

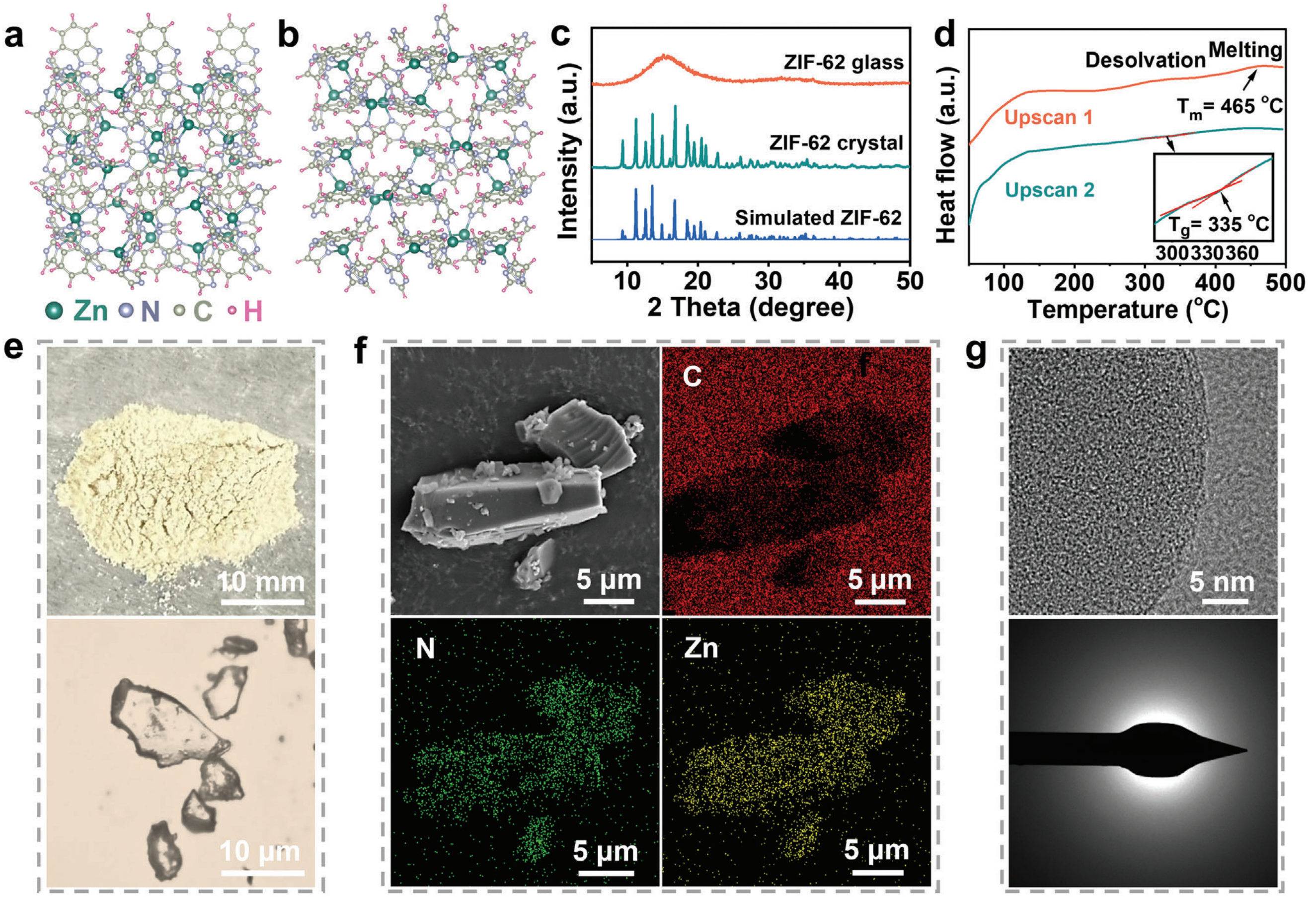

**Figure 2.** Molecular structure model of a) crystalline ZIF-62 and b) glassy ZIF-62; c) XRD patterns of glassy, crystalline, and simulated ZIF-62; d) DSC curves of crystalline ZIF-62 at different upscans; e) and f) Photo, optical, SEM images and EDS mappings of ZIF-62 glass after grinding; g) HRTEM and SEAD images of glassy ZIF-62.

melting of crystalline ZIF-62 (Figure 2d). The glass transition phenomenon is observed at 335 °C in the upscan 2 curve (inset of Figure 2d), meaning crystalline ZIF-62 has transformed into glassy sample, i.e., ZIF-62 glass, after quenching. The results are consistent with the previous reports.[11] Despite the discrepancy in phases between glassy and crystalline ZIF-62, they display parallel Fourier transform infrared spectroscopies (FTIR) (Figure S1, Supporting Information). Especially, typical functional groups including C═N (1670 $cm^{-1}$), C═C (1477 $cm^{-1}$), C─N (1242 $cm^{-1}$), and C─H (748 $cm^{-1}$) are all reserved in ZIF-62 glass after vitrification,[12] suggesting only the emergence of physical change. The $^{13}C$ nuclear magnetic resonance (NMR) peaks assigned to glassy ZIF-62 become wider with various slight shifts in contrast with the crystalline sample (Figure S2, Supporting Information), which means that the chemical environment varies from that before the melt-quenching process despite the only physical change. The X-ray photoelectron spectroscopies (XPS) bands of C, N, and Zn orbitals in the vitrified ZIF-62 also show slight shifts compared with those of ZIF-62 crystal, further implying the changed chemical coordination environment after vitrification (Figure S3, Supporting Information). The varied chemical environment stems from the disruption of Zn─N coordination bond and structural deformation of ZIF-62 glass. As portrayed in Figure S4 (Supporting Information), glassy ZIF-62 immersed in water for 30 days still presents similar XRD patterns with the freshly vitrified ZIF-62, which signifies the splendid stability to water as an SSE matrix.

The as-obtained ZIF-62 glass presents a powdery state with a milky white color after grinding and good transparency in the optical microscope (Figure 2e). Scanning electron microscopy (SEM) image of crystalline ZIF-62 displays an octahedral shape with well-distributed C, N, and Zn elements according to energy dispersive spectrometry (EDS) mappings (Figure S5, Supporting Information). Owing to the fusion, ZIF-62 glass takes on an irregular bulky block despite the uniform distribution of C, N, and Zn, as shown in Figure 2f. Because the vitrified ZIF-62 cannot be damaged by the electron beam at an accelerating voltage of 200 kV,[13] high-resolution transmission electron microscopy (HRTEM) was conducted to probe its microstructural texture. HRTEM image of glassy ZIF-62 shows distorted grains with halo-like selected area electron diffraction (SAED) patterns (Figure 2g), further indicative of long-range disorder characteristics of glassy materials.[14] ZIF-62 glass shows a lower Brunauer-Emmett-Teller (BET) surface area (e.g., 8.43 $m^2$ $g^{-1}$) (Figure S6, Supporting Information) compared with that (e.g., 61.31 $m^2$ $g^{-1}$) of the crystalline polymorph (Figure S7, Supporting

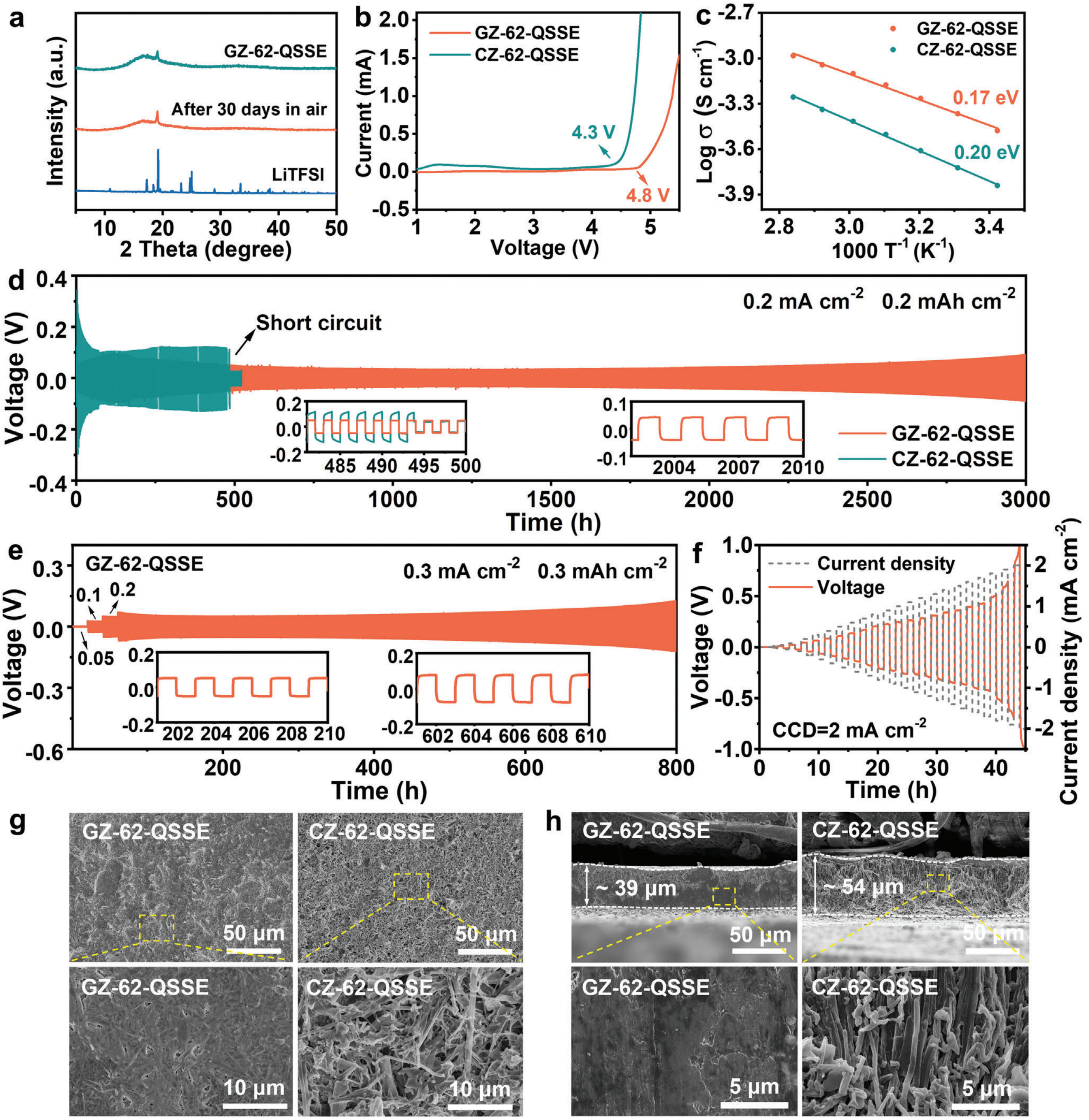

**Figure 3.** a) XRD patterns of LiTFSI and GZ-62-QSSE film before and after exposure for 30 days in air, respectively; b) LSV curves of the Li|GZ-62-QSSE|ss and Li|CZ-62-QSSE|ss cell; c) Arrhenius plots of GZ-62-QSSE and CZ-62-QSSE; d,e) Long-term cycling of symmetric Li|GZ-62-QSSE|Li and Li|CZ-62-QSSE|Li batteries at 0.2 and 0.3 mA cm$^{-1}$; f) CCD measurement of Li|GZ-62-QSSE|Li cell; g,h) Top-view and cross-sectional SEM images of deposited Li layer on Cu foil after plating for 10 h at 1 mA cm$^{-2}$ in Li||Cu battery with GZ-62-QSSE and CZ-62-QSSE, respectively.

Information). These results hint that vitrification causes the porosity reduction resulting from pore collapse and structural densification of ZIF-62.[15]

In view of the superiority of ZIF-62 glass in ionic conduction, it was prepared into membranes with a thickness of ≈74 μm to assess the potential as an SSE matrix (Figure S8, Supporting Information). The as-obtained glassy ZIF-62 film appears a relatively flat and compact surface. The solvent content determined in SSE is 23.1 wt.% according to thermogravimetric analysis (TGA), as revealed in Figure S9 (Supporting Information). After exposure in the air over 30 days, the XRD pattern of GZ-62-QSSE film is in well agreement with that of the fresh sample (**Figure 3a**), indicating its prominent air stability. As is well known, sulfide and halide electrolytes are too sensitive to oxygen and humidity in the air despite their high ionic conductivity;[16] $Li_2CO_3$ is generated on the surface of oxide-based electrolytes if exposed too long in the air.[17] Therefore, the superb air stability of GZ-62-QSSE is a potential advantage, which is beneficial to the massive production, transport, and storage of SSE for battery manufacturers. The linear sweep voltammetry (LSV) profile of GZ-62-QSSE shows a higher upper limit of voltage to 4.8 V in contrast with that (e.g., 4.3 V) of crystalline ZIF-62 quasi-solid-state electrolyte (CZ-62-QSSE) (Figure 3b), suggesting that GZ-62-QSSE has a better antioxidation ability. The occurrence of the bulge at ≈1.3 V and low oxidation voltage for CZ-62-QSSE arises from unstable electrochemical sites such as grain boundaries and dislocations in polycrystals.[18] The ionic resistance property was investigated by electrochemical impedance spectroscopy (EIS). Nyquist plots of ss|GZ-62-QSSE|ss (ss: stainless steel) are all composed of merely an oblique line within the frequency range of 1–$10^6$ Hz under 20–80 °C and the corresponding ionic resistances are lower than those of ss|CZ-62-QSSE|ss (Figures S10 and S11, Supporting Information). The measured ionic conductivity of GZ-62-QSSE is $3.32 \times 10^{-4}$ S $cm^{-1}$ at 20 °C, superior to that of CZ-62-QSSE ($1.44 \times 10^{-4}$ S $cm^{-1}$). $E_a$, the migration barrier for $Li^+$, was calculated according to the Arrhenius equation. The corresponding $E_a$ value of GZ-62-QSSE is 0.17 eV, slightly lower than that of CZ-62-QSSE (0.20 eV) (Figure 3c). This is in well agreement with the results of theoretical calculations. The ionic resistances were also compared before and after folding GZ-62-QSSE film, which lightly increased from 10.02 to 10.71 Ω (Figures S12 and S13, Supporting Information), implying that GZ-62-QSSE owns good flexibility and stable continuous structure.

To further estimate the migration capability, $t^+$ was determined in accordance with the Bruce-Vincent-Evans (BVE) method.[8] GZ-62-QSSE shows a high $t^+$ of 0.74, while the $t^+$ value of CZ-62-QSSE is only 0.47 (Figures S14 and S15, Supporting Information). To explain more than 1.5-time increase in $t^+$ for GZ-62-QSSE, binding energy (BE) between bis(trifluoromethanesulfonyl) imide anions ($TFSI^-$) and MOFs was calculated in accordance with the simplified structural models. BE of the disrupted-linker ZIF-62 model, representing GZ-62-QSSE with incompletely coordinated $Zn^{2+}$, is 4.44 eV, outclassing that of CZ-62-QSSE (0.78 eV), as shown in Figure S16 (Supporting Information). Intensively immobilizing $TFSI^-$ by the plenty of uncoordinated $Zn^{2+}$ increases $Li^+$ mobility in the deformed GZ-62-QSSE structure. Higher BE between $Li^+$ and crystalline ZIF-62 is 2.91 eV compared with those of glassy counterpart (0.21 eV), also indicative of high $Li^+$ motion in GZ-62-QSSE. High $t^+$ implies high C-rate performance of batteries when the differences in SSE conductivity are moderate. The symmetric Li|SSE|Li cell was assembled to appraise the polarization and compatibility with the Li anode through a plating/stripping test. As shown in Figure 3d, the stable polarization voltage of ≈34.1 mV lasts 1750 h and then slowly increases to 90.5 mV after 3000 h at 0.2 mA $cm^{-2}$ and 0.2 mAh $cm^{-2}$ for GZ-62-QSSE. By contrast, the voltage of the CZ-62-QSSE cell fast decreases from the initial 112.1 mV and is confronted with a short-circuit phenomenon for less than 500 h. After a stepwise activation from 0.05 to 0.2 mA $cm^{-2}$ for 100 h, GZ-62-QSSE also exhibits a stable polarization voltage of 51.6 mV over the subsequent 400 h and tardily increases to 126.6 mV after 800 h under 0.3 mA $cm^{-2}$ and 0.3 mAh $cm^{-2}$ (Figure 3e). The critical current density (CCD) that GZ-62-QSSE can endure is 2 mA $cm^{-2}$, whereas that of CZ-62-QSSE is only 0.7 mA $cm^{-2}$ (Figure 3f; Figure S17, Supporting Information). The measured current density ($J_0$) for GZ-62-QSSE is $3.98 \times 10^{-4}$ mA $cm^{-2}$, evidently lower than that of CZ-62-QSSE (e.g., $5.25 \times 10^{-4}$ mA $cm^{-2}$), illustrating that GZ-62-QSSE bears higher corrosion resistance (Figure S18, Supporting Information). This means the presence of a larger kinetic barrier for electrons in the GZ-62-QSSE cell in comparison with the CZ-62-QSSE cell.[19] To further investigate Li plating/stripping behaviors, asymmetric Li||Cu batteries with different electrolytes were assembled. The nucleation overpotential is 42.9 mV for GZ-62-QSSE, smaller than that (e.g., 54.7 mV) of CZ-62-QSSE (Figure S19, Supporting Information). The Li plating/stripping reversibility can be reflected by Coulombic efficiency (CE). Although much lower CE is delivered in the first 30 cycles possibly due to the irreversible reaction between $Li^+$ and defects in ZIF-62 glass, it gradually increases CE from 47.5% to 95.6% over 200 cycles. In stark contrast, the CE of CZ-62-QSSE decays rapidly to less than 10% in spite of the high initial value of 88.9% (Figure S20, Supporting Information). As shown in top-view SEM images of the deposited Li, the coarse and loose surface with many pores is observed on Cu foil, and the Li dendrites are generated as a consequence of uneven Li deposits in CZ-62-QSSE cell (Figure 3g). In sharp comparison with GZ-62-QSSE, a flat and dense plated layer without dendrite is formed on Cu foil under the same condition. From the cross-sectional SEM image of the plated Li metal, the loose texture with a thickness of 54 µm is present in Li|CZ-62-QSSE|Cu, whereas the compact equivalent in Li|GZ-62-QSSE|Cu is only 39 µm (Figure 3h). Such homogeneous plating/stripping behavior of GZ-62-QSSE is rooted in its low migration barrier, and these features ensure the same and fast ion transport. Abundant N species from imidazole and benzimidazole linkers in GZ-62-QSSE can also guide the ordered Li plating through chemical interaction.[20]

The comprehensive advantages of our designed SSE are finally embodied in the performance of full cells. To demonstrate the practicability and versatility of GZ-62-QSSE electrolyte, full cells coupled with LFP, NCM811, and $LiCoO_2$ (LCO) as cathodes were evaluated, respectively. As showcased in Figure S21 (Supporting Information), LFP|GZ-62-QSSE|Li cell can release 156.5 mAh $g^{-1}$ at 0.1 C. Even at larger current densities, the cell shows higher capacities than those of LFP|CZ-62-QSSE|Li cells. Especially at 5 C, the GZ-62-QSSE cell still delivers a higher capacity of 83.6 mAh $g^{-1}$ with clear charge/discharge plateaus (Figure S22, Supporting Information), outperforming the CZ-62-QSSE cell. In contrast with the reported MOF-based electrolytes, the high C-rate performance of GZ-62-QSSE exceeds those of many previous reports, as shown in Figure S23 and Tables S1 and S2 (Supporting Information). Such rate-capability fully highlights the remarkable fast-charging ability of GZ-62-QSSE rooting from fast $Li^+$ motion and high $t^+$. Capacity retention is another important indicator in the comprehensive evaluation of LMBs. Therefore, long-cycling performances were investigated at 1 C and 3 C (25 °C), respectively. After the initial two-cycle activation at 0.1 C, LFP|GZ-62-QSSE|Li shows an incipient capacity of 132.1 mAh $g^{-1}$ and a capacity retention of 72.6% after 3000 cycles at 1 C (**Figure** 4a; Figure S24, Supporting Information). As a comparison, LFP|CZ-62-QSSE |Li undergoes a fast and severe capacity fade despite displaying a preliminary capacity of 123.6 mAh $g^{-1}$. Our proposed ZIF-62

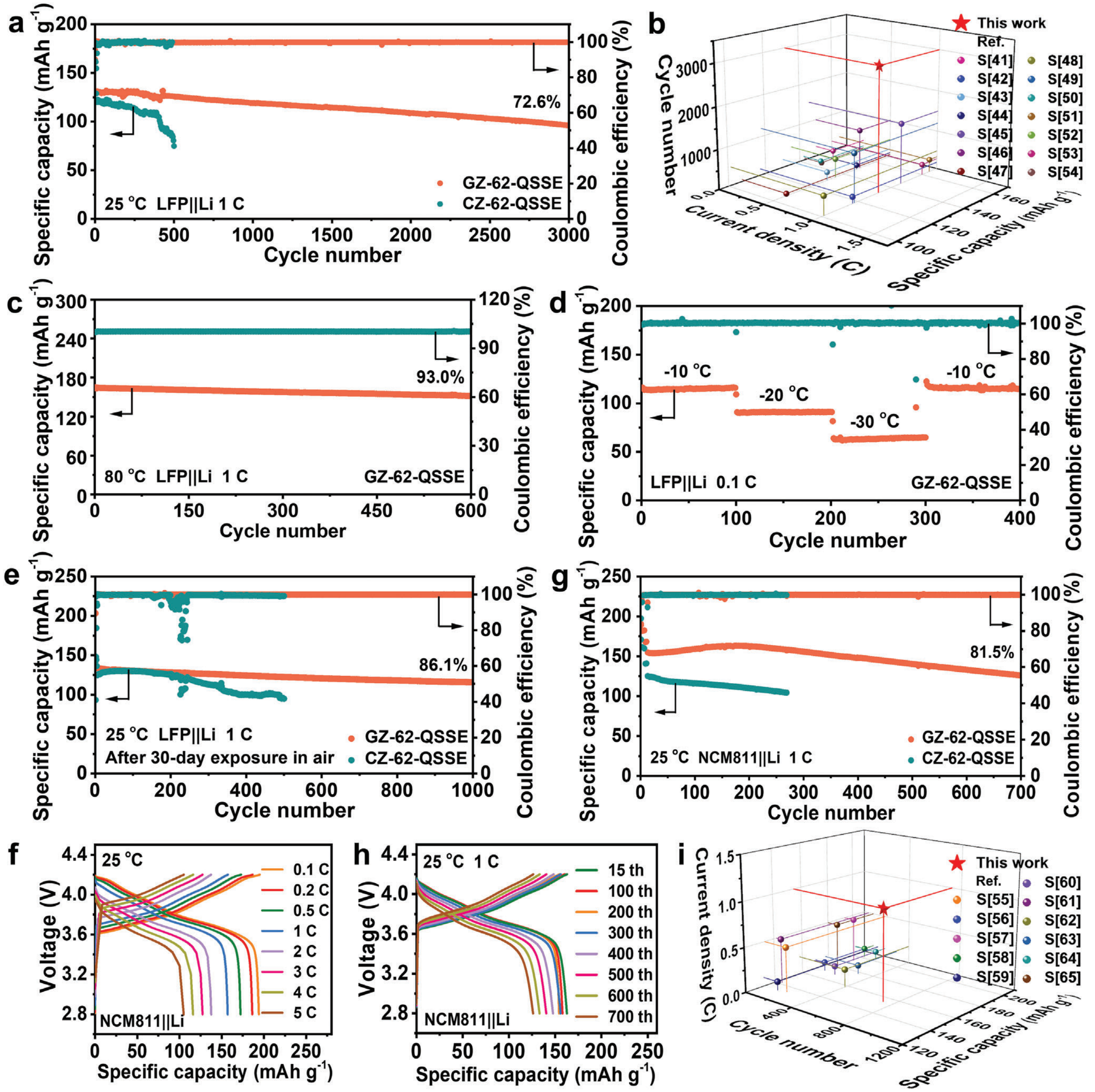

**Figure 4.** a) Galvanostatic cycling performances of LFP|GZ-62-QSSE|Li and LFP|CZ-62-QSSE|Li cells at 1 C and 25 °C; b) Performance comparison of LFP|GZ-62-QSSE|Li with the previously reported other MOF-based SSEs matched with LFP; c,d) Cycling performance of LFP|GZ-62-QSSE|Li cell at 80 °C and −10–−30 °C; e) Cycling stability of LFP||Li cell employed GZ-62-QSSE and CZ-62-QSSE exposed in air over 30 days; f,h) Galvanostatic charge/discharge profiles of NCM811|GZ-62-QSSE|Li cell at various current densities and 1 C, respectively; g) Cycling stability of NCM811|GZ-62-QSSE|Li and NCM811|CZ-62-QSSE|Li cells at 1 C and 25 °C; i) Performance comparison of NCM811|GZ-62-QSSE|Li with the previously reported other SSEs matched with NCM811.

glass-based batteries deliver ultralong-term stability with an ultralow capacity decay rate of 0.009% (Figure 4b; Tables S3 and S4, Supporting Information). Likewise, a high initial capacity of 101.3 mAh g$^{-1}$ with a retention of 81.7% at 3 C over 800 cycles is shown for LFP|GZ-62-QSSE|Li in Figure S25 (Supporting Information), while LFP|CZ-62-QSSE|Li cell bears a rapid capacity decline with 60.7 mAh g$^{-1}$ and a retention of 63.8% for less than 600 cycles. At a higher cathodic loading of ≈5 mg cm$^{-2}$, the GZ-62-QSSE cell exhibits a rather high and steady capacity of 153.3 mAh g$^{-1}$ with a splendid retention of 96.8% at 0.2 C after 450 cycles (Figure S26, Supporting Information).

The temperature endurance is a vital factor of environmental adaptation for batteries. Surprisingly, LFP|GZ-62-QSSE|Li can function well at the wide temperature range from −30 to 80 °C. At 80 °C, the cell releases a capacity of 163.5 mAh $g^{-1}$ with an excellent retention of 93% for 600 cycles at 1 C, as shown in Figure 4c. At −10 and −30 °C, GZ-62-QSSE still possesses ionic conductivities of $9.30 \times 10^{-5}$ and $1.45 \times 10^{-5}$ S $cm^{-1}$, respectively (Figure S27, Supporting Information). Impressively, LFP|GZ-62-QSSE|Li still delivers stable capacities of 117.1, 91.9, and 62.9 mAh $g^{-1}$ at 0.1 C under −10, −20 and −30 °C for every 100 cycles, respectively (Figure 4d). When the temperature is returned to −10 °C, the capacity basically recovers to 117.8 mAh $g^{-1}$ with admirable reversibility. These demonstrate that GZ-62-QSSE has an outstanding temperature adaptability due to the prominent ionic conductivity of GZ-62-QSSE. Amazingly, GZ-62-QSSE exposed for 30 days in the air was employed in LFP||Li cell and delivers a remarkable cycling performance with an incipient capacity of 134.3 mAh $g^{-1}$ with retention of 86.1% over 1000 cycles, as described in Figure 4e. In contrast, LFP|CZ-62-QSSE|Li undergoes fast capacity decay compared with LFP|GZ-62-QSSE|Li despite the parallel specific capacity in the initial 200 cycles. These results demonstrate that GZ-62-QSSE owns unparalleled air stability without undermining the electrochemical performance. Figures 4f and S28 (Supporting Information) further reveal the disparity of their rate capability for GZ-62-QSSE and CZ-62-QSSE matched with NCM811. NCM811|GZ-62-QSSE|Li discharges higher capacities than its control group, especially at 2–5 C. For instance, the cell equipped with the glassy electrolyte exhibits 105.1 mAh $g^{-1}$ at 5 C, far surpassing NCM811|CZ-62-QSSE|Li (e.g., 22.1 mAh $g^{-1}$). In Figure 4g,h, NCM811|GZ-62-QSSE|Li suffers a rapid capacity decay because of structural degradation in cathodes, including dissolution of transition metal ions, cracking, oxygen loss, and phase transition to a rock salt structure.[21] But NCM811|GZ-62-QSSE|Li still runs for 700 cycles with a starting capacity of 154.5 mAh $g^{-1}$ and a capacity retention of 81.5% and the corresponding CE is kept near 100%. With regard to the outstanding cycling performance of GZ-62-QSSE paired with NCM811, GZ-62-QSSE overmatches many previously reported QSSEs, as shown in Figure 4i, further illustrating its enormous advantage as an electrolyte. As for cells matching with LCO, the rate capability of LCO|CZ-62-QSSE|Li (e.g., 45.2 mAh $g^{-1}$ at 5 C) is inferior to that of LCO|GZ-62-QSSE|Li (e.g., 83.4 mAh $g^{-1}$ at 5 C), as revealed in Figure S29 (Supporting Information). LCO|GZ-62-QSSE|Li exhibits a capacity of 124.8 mAh $g^{-1}$ with a retention of 90.0% at 1 C for 250 cycles (Figure S30, Supporting Information). In sharp contrast, a rapid capacity decay from 121.2 to 70.6 mAh $g^{-1}$ happens to LCO|CZ-62-QSSE|Li under the same conditions, demonstrating that GZ-62-QSSE prevails over its control group, again.

To trace the origin of excellent cycling stability of LFP|GZ-62-QSSE|Li, SEM, TEM, and XPS data of the cycled electrodes were examined in detail. As revealed in Figure S31 (Supporting Information), LFP cathode contacting with GZ-62-QSSE maintains a continuous and intact surface after cycling and forms a stark contrast with LFP cathode in LFP|CZ-62-QSSE|Li, where the observable cracks are present. In **Figure** 5a, a clear CEI layer with a thickness of ≈4 nm tightly wraps on an LFP particle contacting with GZ-62-QSSE, however, an uneven CEI film is generated in LFP|CZ-62-QSSE|Li (Figure S32, Supporting Information). As seen from Li, C, and F elements XPS spectra in Figure 5b, Figures S33 and S34 (Supporting Information), their CEI layers both comprise inorganic compounds including LiF and $Li_2O$ and organic component $ROCO_2Li$, derived from the decomposition of triethylene glycol monomethyl ether, propylene carbonate, and Li salt. The corresponding proportions were counted in Figure 5c. Interestingly, LiF content (13%) in CZ-62-QSSE is slightly higher than that of GZ-62-QSSE (11%), whereas $Li_2O$ percentage (50%) is markedly inferior to that of GZ-62-QSSE (60%). For GZ-62-QSSE, the total inorganic content is 71%, significantly exceeding that (63%) of CZ-62-QSSE. Although it is established that LiF bears superior conductivity for ions, high-content $Li_2O$ plays a decisive critical role in fast ionic migration kinetics, as evidenced by the outstanding rate performance for GZ-62-QSSE cell. This agrees well with the boost of ionic mobility in previous reports.[22] A proper content of organic components can reinforce the CEI toughness from GZ-62-QSSE, which avoids CEI rupture during lithiation/delithiation.[23] Instead, the excessive organic composition lowers ionic movement as a result of the thermal motion of chain segments. On the contrary, CEI in CZ-62-QSSE undergoes repetitive rupture and reconstruction, which is reflected by the SEM image of the LFP cathode against CZ-62-QSSE to a certain extent (Figure S31b, Supporting Information). Owing to the repeated crack and regeneration of CEI, LiTFSI is continuously consumed, as proved by a higher LiF proportion in CEI from CZ-62-QSSE (Figure S34, Supporting Information). As for Li anodes toward SSEs, the cycled Li from LFP|GZ-62-QSSE|Li has a flat surface while the counterpart Li in LFP|CZ-62-QSSE|Li showcases a coarse surface resulting from uneven Li deposition with severe dendrites (Figure 5d; Figure S35, Supporting Information). This phenomenon stems from different $Li^+$ migration rates in ZIF-62 crystal. From XPS data, SEI is also composed of LiF, $Li_2O$, and $ROCO_2Li$ (Figure 5e; Figures S36 and S37). Resembling with CEI, the total inorganic content (61%) in CZ-62-QSSE is obviously less than that (74%) of equivalent for GZ-62-QSSE (Figure 5f). XPS depth profiles analysis of CEI and SEI shows that the content of LiF and $Li_2O$ inorganic components increases and the content of $ROCO_2Li$ organic part decreases with the increase of etching depth of CEI and SEI layers (Figures S38 and S39, and Tables S5 and S6, Supporting Information). To better understand the composition features of CEI and SEI, the corresponding models are depicted in Figure 5g. The whole ionic conductivity in a cell depends on a cascade structure comprising of SEI, SSE, and CEI (Figure 5h). Even if SSE possesses an outstanding conductivity for ions, either of SEI and CEI underperforming in ionic transport will impair the electrochemical performance inclusive of rate performance. Our fabricated GZ-62-QSSE contacting Li anode and LFP cathode produces inorganics-dominated electrolyte/electrode interphase, and the formed cascade structure guarantees the unblocked ion transfer for the smooth charge/discharge of batteries.

Flame retardation of SSE is also be of prime importance for battery security. As portrayed in Figure S40 (Supporting Information), GZ-62-QSSE film cannot be ignited by flame within 5 s and also does not burn once withdrawn from fire, implying its excellent flame-retardant property. The pouch cell was assembled with GZ-62-QSSE film and LFP mass loading of 1.5 mg $cm^{-2}$ to

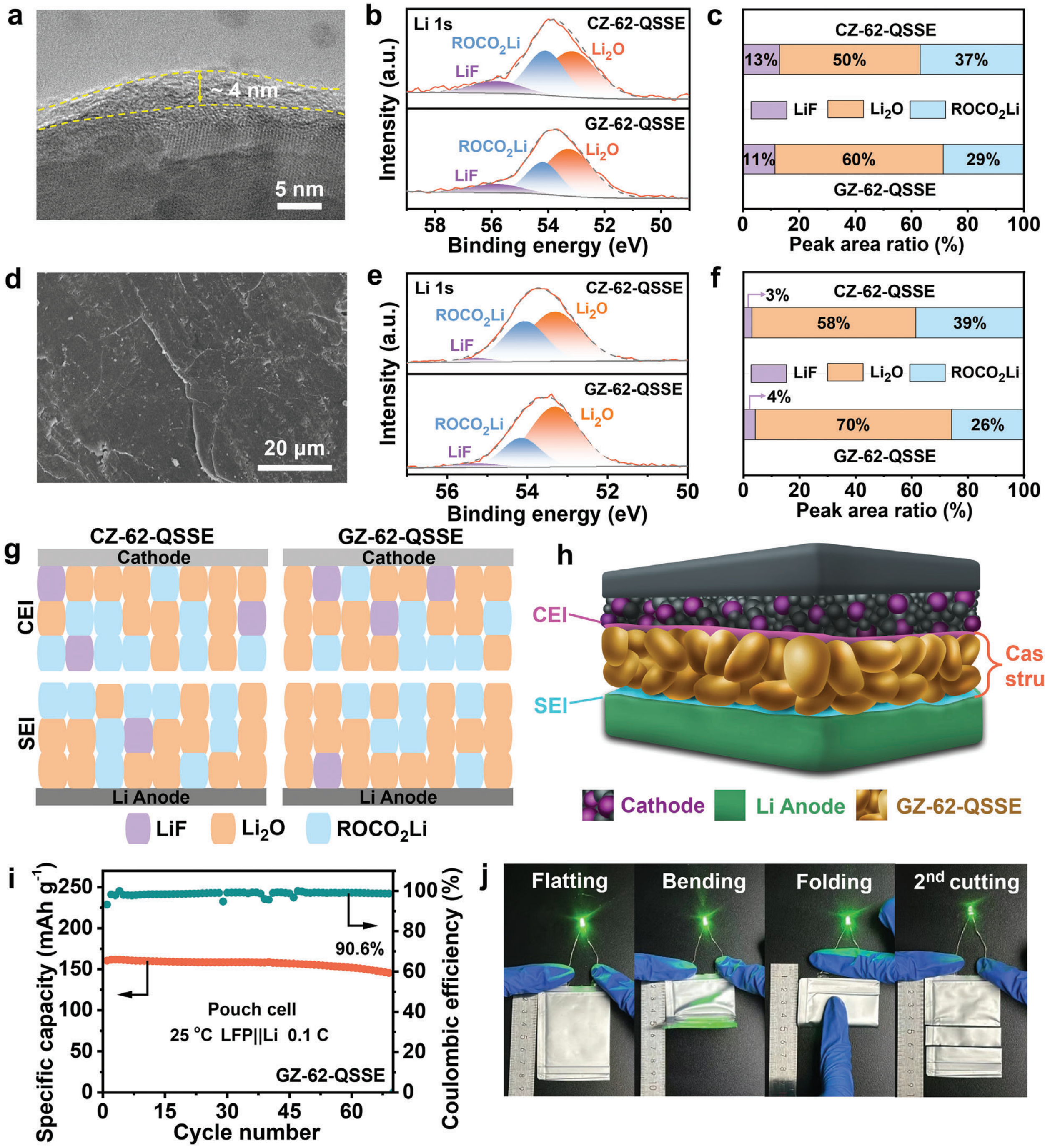

**Figure 5.** a) TEM image of the cycled LFP against GZ-62-QSSE; b) XPS data of Li 1s from CEI on LFP; c) Content of every component in CEI layer; d) SEM image of the cycled Li anode; e) XPS data of Li 1s from SEI on Li anode; f) Content of every component in SEI layer; g) Composition models of CEI and SEI on cathodes and anodes against CZ-62-QSSE and GZ-62-QSSE; h) Cascade structure of SEI, SSE and SEI; i) Cycling performance of LFP|GZ-62-QSSE|Li pouch cell and j) Power supply of LFP|GZ-62-QSSE|Li pouch cell under abuse conditions.

further testify its commercial practicability and discharges 160.7 mAh g$^{-1}$ at 0.1 C for 70 cycles with retention of 90.6% (Figure 5i). Moreover, the pouch cell can power a light-emitting diode (LED), even under abuse conditions inclusive of bending with 90°, folding, and cutting (Figure 5j), further demonstrating the high safety of GZ-62-QSSE.

## 3. Conclusion

To summarize, we elucidate that Li$^+$ migration is accomplished by the N sites from imidazole and benzimidazole ligands in the vitrified ZIF-62 like relay race process and propose GZ-62-QSSE for long-cycling and high-performance LMBs. Theoretical calculations corroborate that ZIF-62 glass can promote $Li^+$ motion in comparison with its crystalline counterpart due to the distorted coordination environment in the glassy sample. The experimental results also demonstrate that glassy ZIF-62 plays important roles in promoting $Li^+$ conduction, modulating even Li deposits, and enhancing flame retardation. Consequently, GZ-62-QSSE owns remarkable ionic conductivity ($3.32 \times 10^{-4}$ S $cm^{-1}$ at 20 °C), a high $t^+$ of 0.74, and outstanding dendrite inhibition. GZ-62-QSSE cells paired with LFP, NCM 811and LCO three cathodes can cycle 3000, 700, and 250 times with 132.1, 154.5, and 124.8 mAh $g^{-1}$ at 1 C. At 5 C, LFP, NCM811, and LCO cells discharge 83.6, 105.1, and 83.4 mAh $g^{-1}$, respectively. After 30 days of exposure to air, LFP||Li cell utilizing GZ-62-QSSE delivers a remarkable incipient capacity of 134.3 mAh $g^{-1}$ with retention of 86.1% over 1000 cycles, demonstrating that GZ-62-QSSE owns unparalleled air stability. Our findings offer an impetus for quasi-solid-state LMBs and may open a fertile ground for exploring advanced solid electrolytes.

## Supporting Information

Supporting Information is available from the Wiley Online Library or from the author.

## Acknowledgements

The fundings from the National Natural Science Foundation of China (Nos. 52371224; 52322203), the Talent Project Grants of University of Science and Technology Liaoning (6003000341), and the Fundamental Research Funds of Education Bureau of Liaoning Province (JYTMS20230945) are gratefully acknowledged.

## Conflict of Interest

The authors declare no conflict of interest.

## Data Availability Statement

The data that support the findings of this study are available from the corresponding author upon reasonable request.

## Keywords

interphase, lithium metal batteries, MOF glass, solid-state electrolytes, ZIF-62

Received: November 27, 2024
Revised: January 22, 2025
Published online:

---

[1] a) C. Xie, C. Wang, Y. Xu, T. Li, Q. Fu, X. Li, *Nat. Energy* **2024**, *9*, 714; b) C. Wang, C. Wang, M. Li, S. Zhang, C. Zhang, S. Chou, J. Mao, Z. Guo, *Mater. Today* **2024**, *72*, 235; c) X. Xu, J. Chen, J. Li, Z. Wang, J. Shen, P. Lin, J. Sun, B. Huang, T. Zhao, *Adv. Funct. Mater.* **2024**, https://doi.org/10.1002/adfm.202415298.

[2] a) H. Su, Y. Zhong, C. Wang, Y. Liu, Y. Hu, J. Li, M. Wang, L. Jiao, N. Zhou, B. Xiao, X. Wang, X. Sun, J. Tu, *Nat. Commun.* **2024**, *15*, 2552; b) T. Dai, S. Wu, Y. Lu, Y. Yang, Y. Liu, C. Chang, X. Rong, R. Xiao, J. Zhao, Y. Liu, W. Wang, L. Chen, Y. Hu, *Nat. Energy* **2023**, *8*, 1221; c) X. Lin, Y. Zhao, C. Wang, J. Luo, J. Fu, B. Xiao, Y. Gao, W. Li, S. Zhang, J. Xu, F. Yang, X. Hao, H. Duan, Y. Sun, J. Guo, Y. Huang, X. Sun, *Angew. Chem., Int. Ed.* **2024**, *63*, 202314181.

[3] S. Horike, N. Ma, Z. Fan, S. Kosasang, M. M. Smedskjaer, *Nano Lett.* **2021**, *21*, 6382.

[4] J. Ding, T. Du, L. R. Jensen, S. S. Sorensen, D. Wang, S. Wang, L. Zhang, Y. Yue, M. M. Smedskjaer, *Adv. Mater.* **2024**, *36*, 2400652.

[5] X. Wang, D. Guan, C. Miao, J. Li, J. Li, X. Yuan, X. Ma, J. Xu, *Adv. Energy Mater.* **2024**, *14*, 2303829.

[6] a) J. Ding, T. Du, E. H. Thomsen, D. Andresen, M. R. Fischer, A. K. Møller, A. R. Petersen, A. K. Pedersen, L. R. Jensen, S. Wang, M. M. Smedskjaer, *Adv. Sci.* **2024**, *11*, 2306698; b) C. Gao, Z. Jiang, S. Qi, P. Wang, L. R. Jensen, M. Johansen, C. K. Christensen, Y. Zhang, D. B. Ravnsbaek, Y. Yue, *Adv. Mater.* **2022**, *34*, 2110048; c) J. Yan, C. Gao, S. Qi, Z. Jiang, L. R. Jensen, H. Zhan, Y. Zhang, Y. Yue, *Nano Energy* **2022**, *103*, 107779.

[7] S. Liu, G. Jiang, Y. Wang, C. Liu, T. Zhang, Y. Wei, B. An, *ACS Nano* **2024**, *18*, 14907.

[8] G. Jiang, C. Qu, F. Xu, E. Zhang, Q. Lu, X. Cai, S. Hausdorf, H. Wang, S. Kaskel, *Adv. Funct. Mater.* **2021**, *31*, 2104300.

[9] a) H. Cheng, J. Cao, F. Li, X. Geng, D. Li, Y. Wei, X. Lin, H. Xu, Y. Huang, *Adv. Funct. Mater.* **2024**, *34*, 2307677; b) Y. Li, F. Bai, C. Li, Y. Wang, T. Li, *Adv. Energy Mater.* **2024**, *14*, 2304414.

[10] a) N. Adelstein, B. C. Wood, *Chem. Mater.* **2016**, *28*, 7218; b) M. Chai, R. Chen, K. Xu, Y. Chen, S. Ma, R. Lin, V. Chen, J. Hou, *J. Mater. Chem. A* **2023**, *11*, 20302.

[11] Y. Wang, H. Jin, Q. Ma, K. Mo, H. Mao, A. Feldhoff, X. Cao, Y. Li, F. Pan, Z. Jiang, *Angew. Chem., Int. Ed.* **2020**, *59*, 4365.

[12] X. Miao, P. Wang, R. Sun, J. Li, Z. Wang, T. Zhang, R. Wang, Z. Li, Y. Bai, R. Hao, L. Yin, *Adv. Energy Mater.* **2021**, *11*, 2102396.

[13] O. Smirnova, S. Hwang, R. Sajzew, L. Ge, A. Reupert, V. Nozari, S. Savani, C. Chmelik, M. R. Reithofer, L. Wondraczek, J. Kärger, A. Knebel, *Nat. Mater.* **2024**, *23*, 262.

[14] Z. Yang, Y. Belmabkhout, L. N. McHugh, D. Ao, Y. Sun, S. Li, Z. Qiao, T. D. Bennett, M. D. Guiver, C. Zhong, *Nat. Mater.* **2023**, *22*, 888.

[15] a) H. Tao, T. D. Bennett, Y. Yue, *Adv. Mater.* **2017**, *29*, 1601705; b) T. D. Bennett, S. Horike, *Nat. Rev. Mater.* **2018**, *3*, 431.

[16] a) Y. Nikodimos, S. Jiang, S. Huang, B. Taklu, W. Huang, G. B. Desta, T. M. Tekaligne, Z. B. Muche, K. Lakshmanan, C. Chang, T. M. Hagos, K. N. Shitaw, S. Yang, S. Wu, W. Su, B. Hwang, *ACS Energy Lett.* **2024**, *9*, 1844; b) K. Wang, Z. Gu, H. Liu, L. Hu, Y. Wu, J. Xu, C. Ma, *Adv. Sci.* **2024**, *11*, 2305394; c) X. Wu, Z. Bai, B. Bao, Q. Zhang, W. Jiang, Y. Li, C. Hou, K. Li, H. Wang, *Adv. Funct. Mater.* **2024**, *34*, 2312358; d) C. Wang, J. Liang, J. Luo, J. Liu, X. Li, F. Zhao, R. Li, H. Huang, S. Zhao, L. Zhang, J. Wang, X. Sun, *Sci. Adv.* **2021**, *7*, eabh1896.

[17] N. Wang, M. Jia, Z. Bi, X. Guo, *Adv. Funct. Mater.* **2024**, *34*, 2401400.

[18] a) F. Wu, Z. Chen, S. Fang, W. Zuo, G. Kim, S. Passerini, *Energy Storage Mater.* **2023**, *63*, 103062; b) F. Li, X. Cheng, G. Lu, Y. Yin, Y. Wu, R. Pan, J. Luo, F. Huang, L. Feng, L. Lu, T. Ma, L. Zheng, S. Jiao, R. Cao, Z. Liu, H. Zhou, X. Tao, C. Shang, H. Yao, *J. Am. Chem. Soc.* **2023**, *145*, 27774.

[19] S. Chai, Z. Chang, Y. Zhong, Q. He, Y. Wang, Y. Wan, M. Feng, Y. Hu, W. Li, W. Wei, A. Pan, *Adv. Funct. Mater.* **2023**, *33*, 2300425.

[20] a) C. Li, S. Liu, C. Shi, G. Liang, Z. Lu, R. Fu, D. Wu, *Nat. Commun.* **2019**, *10*, 1363; b) Y. Hu, N. Dunlap, S. Wan, S. Lu, S. Huang, I. Sellinger, M. Ortiz, Y. Jin, S. Lee, W. Zhang, *J. Am. Chem. Soc.* **2019**, *141*, 7518.

[21] W. Li, Z. He, Y. Jie, F. Huang, Y. Chen, Y. Wang, W. Zhang, X. Zhu, R. Cao, S. Jiao, *Adv. Funct. Mater.* **2024**, *34*, 2406770.

[22] a) G. M. Hobold, C. Wang, K. Steinberg, Y. Li, B. M. Gallant, *Nat. Energy* **2024**, *9*, 580; b) H. Zeng, K. Yu, J. Li, M. Yuan, J. Wang, Q. Wang, A. Lai, Y. Jiang, X. Yan, G. Zhang, H. Xu, J. Wang, W. Huang, C. Wang, Y. Deng, S. Chi, *ACS Nano* **2024**, *18*, 1969; c) J. Zhang, S. Li, X. Wang, S. Mao, J. Guo, Z. Shen, J. Mao, Q. Wu, K. Shen, H. Cheng, Y. Tan, Y. Lu, *Adv. Energy Mater.* **2024**, *14*, 2302587.

[23] Y. Sun, J. Li, S. Xu, H. Zhou, S. Guo, *Adv. Mater.* **2023**, *36*, 2311687.